npj | computational materials

Article

Published in partnership with the Shanghai Institute of Ceramics of the Chinese Academy of Sciences

https://doi.org/10.1038/s41524-025-01706-2

High-throughput discovery of perturbation-induced topological magnons

Mohammed J. Karaki[1,5] ✉, Ahmed E. Fahmy[1,5] ✉, Archibald J. Williams[2], Sara Haravifard[3,4], Joshua E. Goldberger[2] & Yuan-Ming Lu[1] ✉

Topological magnons give rise to possibilities for engineering novel spintronics devices with critical applications in quantum information and computation, due to their symmetry-protected robustness and low dissipation. However, to make reliable and systematic predictions about the material realization of topological magnons has been a major challenge, due to the lack of neutron scattering data for most materials and the absence of reliable ab initio calculations for magnons. In this work, we significantly advance the symmetry-based approach for identifying topological magnons through developing a fully automated algorithm, utilizing the theory of symmetry indicators, that enables a highly efficient and large-scale search for candidate materials hosting perturbation-driven topological magnons. This progress not only streamlines the discovery process but also expands the scope of materials exploration beyond previous manual or traditional approaches, offering a powerful tool for uncovering novel topological phases in magnetic systems. Performing a large-scale search over all 1649 magnetic materials in the Bilbao Crystallographic Server (BCS) with a commensurate magnetic order, we discover 387 perturbation-induced topological magnon materials, significantly expanding the pool of topological magnon materials and showing that more than 23% of all commensurate magnetic compounds in the BCS database are topological. We further discuss examples and experimental accessibility of the candidate materials, shedding light on future experimental realizations of topological magnons in magnetic materials. We provide an open-source program that checks the symmetry-enforced magnon band topology of any commensurate magnetic structure upon perturbations and allows researchers to reproduce our results.

The discovery of topological insulators[1] revealed that in electronic materials, symmetry-protected topological surface states can arise from nontrivial Berry phases of electronic bands in the bulk. Beyond electronic band structures, in strongly correlated magnetic materials, similar phenomena can also occur in spin wave excitations of ordered magnets, giving rise to topological magnons[2]. As collective excitations of spin degrees of freedom in magnetically ordered materials, magnons carry energy and spin through the crystal lattice without transporting electric charge, making them potential candidates for low-dissipation information processing[3]. The concept of topology introduces robustness to these excitations, allowing for the existence of magnon modes that are protected against elastic scattering by impurities or defects, making topological magnonics a robust route towards spintronic devices[4]. It is therefore highly desirable to identify a list of material candidates that realize topological magnons.

At the microscopic level, characterizing and understanding the magnon excitations in magnetically ordered structures usually depends on a model spin Hamiltonian that captures spin–spin (and possibly multi-spin) interactions, possible anisotropies, and couplings to external fields. Theoretically solving the spin model can determine the ground-state magnetic order and the magnon spectrum, identify the possible nontrivial topology of the magnon bands, and predict topological surface states therein. In contrast to weakly correlated topological electronic[5–10] and phonon[11] materials, where ab initio calculations have been instrumental in their discovery, strongly correlated magnetic materials present greater challenges for ab

---

[1]Department of Physics, The Ohio State University, Columbus, OH, USA. [2]Department of Chemistry and Biochemistry, The Ohio State University, Columbus, OH, USA. [3]Department of Physics, Duke University, Durham, NC, USA. [4]Department of Mechanical Engineering and Materials Science, Duke University, Durham, NC, USA. [5]These authors contributed equally: Mohammed J. Karaki, Ahmed E. Fahmy. ✉e-mail: karaki.4@osu.edu; abdelazim.2@osu.edu; lu.1435@osu.edu

initio in reliably predicting their magnetic properties. Obtaining such a microscopic spin model has become possible thanks to the increasing development and accessibility of magnetic spectroscopy, specifically Inelastic Neutron Scattering (INS) spectroscopy for bulk structures[12], and other techniques such as Spin-Polarized Electron Energy Loss Spectroscopy (SPEELS) for thin-film structures[13,14]. Additionally, Resonant Inelastic X-ray Scattering (RIXS)[15] was also able to probe magnetic excitations in both thin films[16,17] and bulk structures[18–20].

Due to the difficulty for first principles to accurately predict spin models in strongly correlated magnetic materials, a good microscopic spin model is typically established by fitting experimentally measured magnon dispersion data obtained by the aforementioned spectroscopic measurements. The topology of the magnon bands can also be diagnosed by calculations of the magnon spectra using this model. Identifying materials that can host topological magnons with this approach is extremely limiting, as it relies on the existence of magnon dispersion data, which are not available for the overwhelming majority of magnetic materials. Moreover, fitting the measured magnon dispersion with spin wave theory results can also encounter many challenges, such as overfitting and local minima. These difficulties make this approach not applicable for a large-scale search for topological magnon materials, calling for a different methodology that does not depend on the specific spin model of magnetic materials.

A symmetry-based approach was recently developed by Karaki et al.[21], which searches topological magnons induced by external perturbations using constructed or literature-sourced microscopic spin Hamiltonians. This method starts with identifying the materials that host symmetry-enforced degeneracies in their magnon band structure. By applying external perturbations, including electric fields, magnetic fields, and/or mechanical strains, the original magnetic symmetry of the ordered magnet is broken down to a subgroup, and the protected degeneracy can be lifted, leading to topological gaps in the magnon spectrum. The topological nature of the resulting magnon bands can be diagnosed using the theory of symmetry indicators[22,23] and topological quantum chemistry[24,25] (TQC). Candidate materials for hosting topological magnons are then selected by filtering out those with trivial symmetry indicators for all of their magnetic subgroups. Finally, symmetry-allowed spin models are constructed for the candidate materials to examine the potential emergence of topological magnons induced by external perturbations. Applying this approach to all of the 23 magnetic insulators in Bilbao Crystallographic Server (BCS) that remain ordered at room temperature, 12 materials were predicted to host field-induced topological magnons[21].

However, this symmetry-based approach necessitates case-by-case examinations and detailed knowledge of spin Hamiltonians for potential candidate materials, which limits its automation and makes large-scale, high-throughput searches for topological magnon materials challenging. This raises the natural question: *Can a symmetry-based approach be developed with a spin-model-independent methodology to facilitate a large-scale material search for topological magnons?* Here, we demonstrate that not only is an efficient and automated search algorithm for topological magnons possible, but it also represents a novel, energetics-free approach for identifying topological phases of matter. By eliminating the need for detailed spin models and leveraging symmetry-based approaches, our algorithm enables large-scale, high-throughput discovery of topological magnon materials, far surpassing traditional methods in both speed and scope. Building on the ideas of TQC and symmetry indicators, we develop a fully automated search algorithm for field-induced topological magnons and carry it out for all materials with commensurate magnetic order in BCS. Among all 1649 commensurate magnetic materials in BCS, we identified 387 candidates (~23.4%) that host field-induced topological magnons. Flowchart Fig. 1 summarizes the conventional approach to identify topological magnons and the shortcut enabled by our algorithm, presented in the workflow diagram Fig. 2.

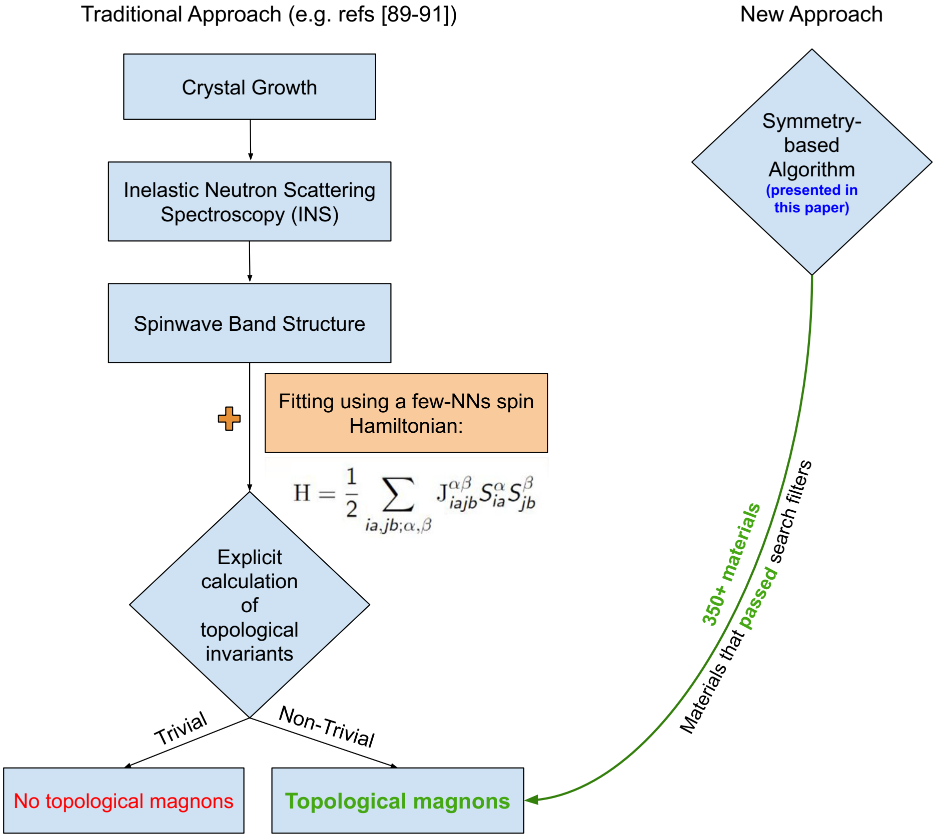

Fig. 1 | Flowchart summarizing the overall goal of the search algorithm developed in this paper. On the left is the conventional approach[89–91] used to identify topological magnon phases (including non-type-I topological magnons identified in ref. 21, where spin models were based on INS previous fittings or theoretically constructed, and band topology was diagnosed through nontrivial $\mathcal{SI}$ values). An alternative approach is introduced through the symmetry-based analysis presented in this work, where more than 350 materials, out of the 1649 commensurate magnetic materials on the BCS MAGNDATA database[32], are found to host field-induced topological magnons.

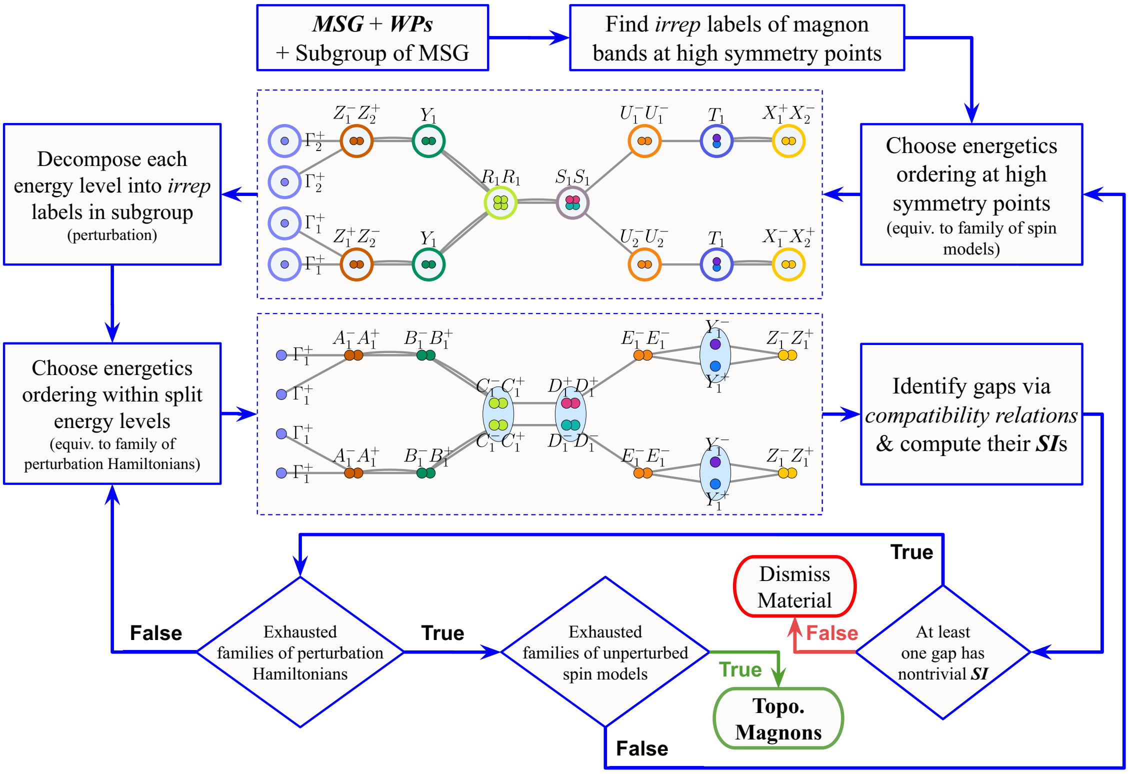

Fig. 2 | Workflow diagram of our developed search algorithm. Flowchart summarizing the automated search algorithm for finding induced nontrivial magnon band topology given a generic magnetically ordered structure. More details about the algorithm architecture, along with its implementation and execution, can be found in the open-source program.

Results

Out of the 1171 magnetic materials in BCS that pass the later-mentioned second filter, 387 successful candidates pass our search algorithm, and therefore they are guaranteed to host topological magnons induced by the relevant perturbations. We present a Supplementary Section 1 where we summarize all topological magnon materials along with an example of the required perturbation to realize a guaranteed topological magnon phase. In subsequent Supplementary Sections (starting from Supplementary Section 3), we provide detailed information on the magnetic structures that passed our search filters. Each section contains the BCS materials that belong to this magnetic structure and subsections of the successful subgroups that met our filtering criteria. Each of those subsections has a list of the possible perturbations required to realize that subgroup, a table of the number of times a given $\mathcal{SI}$ can appear in the magnon spectrum, a table of the possible $\mathcal{SI}$ values for each band gap, and one possible schematic arrangement of the magnon band structure. Each schematic picture (e.g., Supplementary Fig. 7) encodes the unperturbed magnon band representation, *compatibility relations* between *irreps*, the symmetry-lowering process, the induced band gaps, and the $\mathcal{SI}$ values for this particular order of *irreps*. We also provide an open-source code to allow researchers to study the magnon band topology of commensurate magnetic structures.

Computational approach for discovering topological magnons

TQC, reviewed in more detail in the “Methods” section, builds on enumerating all topologically trivial band structures that are smoothly connected to the atomic insulator limit, constructed from a Wannier basis respecting all symmetries of the structure[24,26–29]. For any given space group, the band representations corresponding to a trivial atomic insulator can be identified by checking if a specific band representation belongs to one of the Elementary Band Representations (EBRs) or their composites. If not, the corresponding set of bands is topological. The associated band representations at the high-symmetry points are referred to as Symmetry Indicators ($\mathcal{SI}s$) for band topology[23,30].

Technically, an isolated set of bands is characterized by a *symmetry vector* $\boldsymbol{b} = \{\boldsymbol{n}_{\boldsymbol{k}}^{\boldsymbol{\alpha}}\}$ composed of $\boldsymbol{n}_{\boldsymbol{k}}^{\boldsymbol{\alpha}}$ multiples of irreducible representations (*irreps*) $\boldsymbol{\alpha}$ of the little groups of the distinct high-symmetry momenta $\boldsymbol{k}$ appearing in the set of bands[22,23]. Such a vector is named a *Band Structure*, and its components are constrained by the *compatibility relations* that determine how the *irreps* at the high-symmetry points are connected to those at another **K** point while maintaining the gap condition. The set of all allowed band structures is denoted by $\{\boldsymbol{BS}\}$. A subgroup of $\{\boldsymbol{BS}\}$ is the set of atomic insulators (denoted by $\{\boldsymbol{AI}\}$) that are induced from symmetry-respecting localized Wannier orbitals. Therefore, given a band structure $\boldsymbol{b}$, we can diagnose its topology as follows. If $\boldsymbol{b} \in \{\boldsymbol{BS}\}$ and $\boldsymbol{b} \notin \{\boldsymbol{AI}\}$, these bands are not smoothly connected to the atomic limit and therefore are of nontrivial topology. If $\boldsymbol{b} \in \{\boldsymbol{AI}\}$, then symmetry alone is inconclusive regarding the existence of nontrivial topology. Last, $\boldsymbol{b} \notin \{\boldsymbol{BS}\}$ indicates a violation of the compatibility relations, and therefore, a full gap cannot exist at all high-symmetry points in the BZ.

By allowing components of $\boldsymbol{b}$ to be negative integers, we can define an inverse operation to the direct sum of two representations, and therefore, the sets $\{\boldsymbol{BS}\}$ and $\{\boldsymbol{AI}\}$ are now abelian groups of the same rank. The *SI* group is defined as the quotient group[23]:

$$X_{BS} = \frac{\{\boldsymbol{BS}\}}{\{\boldsymbol{AI}\}} = \mathbb{Z}_{n_1} \times \mathbb{Z}_{n_2} \times \ldots \tag{1}$$

The $\mathcal{SI}s$ for $\mathcal{MSG}s$ have been tabulated in refs. 22,25. This forms a key ingredient to our search algorithm Fig. 2 whose main strategy is to break the $\mathcal{MSG}$ down into a subgroup with a nontrivial $\mathcal{SI}$ group through an external perturbation. Formulas for the $\mathcal{SI}s$ relevant to the materials identified in this work were calculated and listed in Supplementary Section 94. The $\mathcal{SI}$

groups of the perturbation-induced magnon band gaps are then calculated while considering all different orders of the band *irreps* both before and after applying the perturbation. For a given magnetic structure, the magnon band representations, described in more detail in "Methods" section, induced from representations of the magnetic site symmetry groups ($\mathcal{SSG}s$) of the $\mathcal{WP}s$ of the magnetic moments to the full $\mathcal{MSG}$, have been systematically worked out[8,25] and are imported into our search program via the BCS tool MBANDREP[25,31].

Although the induced magnon band representation encodes connectivity of the magnon bands through *compatibility relations* and symmetry-protected degeneracies encoded in the dimension of the *irreps*, it does not determine the energetics of the magnon bands. This leaves each high-symmetry momentum with a number of possibilities originating from the different orderings of *irreps*. Therefore, combining these different orders of *irreps* at the high-symmetry momenta, as long as the *irreps* are connected according to the *compatibility relations*, gives a number of possibilities for the magnon band structure of a given magnetic material. This is why in our search algorithm shown in Fig. 2, it is essential to sweep over all of the different orders of *irreps*. This originates from the lack of spin models and reliable ab initio calculations for magnon band structures, which, if available, would collapse these possibilities to one specific order of *irreps*.

Our automated search algorithm, which is summarized as a flowchart diagram in Fig. 2, proceeds as follows. Firstly, we classify all commensurate magnetic materials from the BCS MAGNDATA tool[32] according to their magnetic structure (i.e., their $\mathcal{MSG}$ and $\mathcal{WP}$). Secondly, we filter out $\mathcal{MSG}s$ whose subgroups that all have a trivial ($\mathbb{Z}_1$) SI group. This constraint excludes 345 out of the 1651 $\mathcal{MSG}s$. Among the 1649 commensurate materials on BCS MAGNDATA[32], 1263 pass this filter. Thirdly, we restrict to $\mathcal{MSG}s$ and $\mathcal{WP}s$ that host symmetry-enforced magnon band degeneracy that can be split upon the application of a symmetry-breaking external perturbation, such as a magnetic field $\boldsymbol{B}$, an electric field $\boldsymbol{E}$, or a mechanical strain $\boldsymbol{\sigma}$. This translates to searching for structures that give rise to at least one multi-dimensional *irrep* that can be decomposed into lower-dimensional *irreps* upon the symmetry-lowering process. Out of the 1263 materials that pass the first filter, 1171 of them pass the second filter and proceed as follows. For a given magnetic structure, the input data consists of two parts: $\mathcal{MSG}$ of the material plus the $\mathcal{WP}$s of its magnetic moments and a symmetry-indicated subgroup of the $\mathcal{MSG}$ corresponding to the perturbation of interest.

The output of the algorithm is a binary result, with two possible outcomes:

Positive: Based solely on the symmetry of the magnetic phase, the material will host topological magnon bands upon the application of the specified perturbation.

Negative: Symmetry is not sufficient to predict topological magnons under the specified perturbation. Topological magnons are not ruled out, but their presence depends on the spin interaction details in the material.

The algorithm proceeds in three main steps:

1. Iterate over different orderings of the original $\mathcal{MSG}$ ***irreps***. This step aims to exhaust all equivalence classes of unperturbed magnon Hamiltonians, where two Hamiltonians are said to belong to the same equivalence class if they share the same energetic ordering of *irreps* at high-symmetry momenta.
2. Iterate over different orderings of *irreps* splitting upon small perturbations. In this step, a perturbation is said to be small if the *irrep* splitting does not, at any momentum $\boldsymbol{k}$, swap the ordering of two subgroup *irreps*. This step is intended to exhaust all equivalence classes of small perturbation Hamiltonians.
3. Identify all gaps and evaluate their SIs. For each energetic ordering associated with a perturbed Hamiltonian, the band gaps are verified by checking whether the collection of bands below a potential gap satisfies the compatibility relations of the subgroup. Concretely, this is decided based on whether the symmetry vector $\overrightarrow{b}$ of these bands belongs to the null space of the compatibility relation matrix $\mathcal{C}$. For each identified gap, we compute its $\mathcal{SI}$[22] to determine if it is topologically nontrivial.

The algorithm terminates in two cases. First, if no gap with nontrivial topology is identified in step (3) for *any* (equivalence class of) perturbed Hamiltonian, the algorithm terminates with a negative result. On the other hand, once all equivalence classes of perturbation Hamiltonians are exhausted (steps 1 and 2) without encountering a termination, the algorithm terminates with a positive result. This exhaustion ensures the existence of at least one topological gap upon applying the relevant perturbation.

Topological magnon compounds

To demonstrate our search results, we discuss two examples in detail, by working out the linear spin wave spectra of their spin Hamiltonians and identifying the magnon band representations therein to validate the predictions of our automated search through calculating the $\mathcal{SI}s$ of the induced magnon band gaps. We focus on two candidate materials, both of which host Weyl points in their magnon spectra, known as Weyl magnons[33,34]. As tabulated in the Supplementary Materials, it turns out that many candidate materials hosting Weyl magnons are characterized by a topological invariant ν, associated with Weyl-$\mathcal{SI}$ groups whose nontrivial values indicate the existence of bulk Weyl points[22] that can either lie on a high-symmetry plane in the Brillouin zone or at generic momenta depending on the $\mathcal{MSG}$, along with surface magnon arcs[21,34] resembling Fermi arcs in electronic Weyl semimetals. In the first example, $NdMnO_3$, we analyze a case where Weyl magnons are $\mathcal{SI}$-signaled to lie on a high-symmetry momentum plane. To validate our prediction based on the tabulated values of the $\mathcal{SI}s$, we build a symmetric spin model, calculate its magnon spectrum, identify Weyl points on that high-symmetry plane, and identify their associated surface magnon arcs after terminating the periodicity of the lattice on one surface. In our second example, Ca_2RuO_4, we encounter a different situation where Weyl points exist at generic momenta, causing different Chern numbers on different planes in the momentum space. For this end, we check that the tabulated $\mathcal{SI}$ of the gap of interest is consistent with explicit calculations of the magnon spectrum. We then identify the Weyl magnons and validate the variance of the Chern numbers between the different high-symmetry planes.

$NdMnO_3$

Our first example is the orthorhombic perovskite $NdMnO_3$, in which Mn^{2+} moments become magnetically ordered below a transition temperature $T_N = 78\,K$[35]. The magnetic structure belongs to $\mathcal{MSG}$ $Pn'ma'$ with the Mn^{2+} ions located at $\mathcal{WP}$ $4b$. The magnetic structure is such that the magnetic moments align antiferromagnetically along the a-axis and acquire a small ferromagnetic component along the b-axis (see Supplementary Fig. 2a). It turns out that below a second transition temperature of around $T_N' = 15K$, the Nd^{4+} moments located at $\mathcal{WP}$ $4c$ become magnetically ordered as well[36]. In the low-temperature phase, the Mn^{2+} moments at $\mathcal{WP}s$ $4b$ and the Nd^{4+} moments $4c$ exhibit long-range magnetic orders. It turns out that both phases pass our filters, hosting topological magnons as detailed in Supplementary Section 76.

Here we focus on the first phase in which only the $4b$ $\mathcal{WP}$ moments are magnetically ordered. The magnon band representation induced from this $\mathcal{WP}$ to the full $\mathcal{MSG}$ is:

$$\begin{aligned}(A_g)_{4b} \uparrow Pn'ma'\,(62.448) = \; & 2\Gamma_1^+(1) \oplus 2\Gamma_2^+(1) \oplus R_1R_1(4) \\ & \oplus S_1S_1(4) \oplus 2T_1(2) \oplus U_1^-U_1^-(2) \\ & \oplus U_2^-U_2^-(2) \oplus X_1^+X_2^-(2) \oplus X_1^-X_2^+(2) \\ & \oplus 2Y_1^-(2) \oplus Z_1^+Z_2^-(2) \oplus Z_1^-Z_2^+(2).\end{aligned} \tag{2}$$

therefore there is a symmetry-enforced four-fold degeneracy at $\mathcal{R}$ and $\mathcal{S}$, two-fold degeneracy at the $\mathcal{T}, \mathcal{U}, \mathcal{X}, \mathcal{Y}, \mathcal{Z}$ and no degeneracy at Γ. Upon

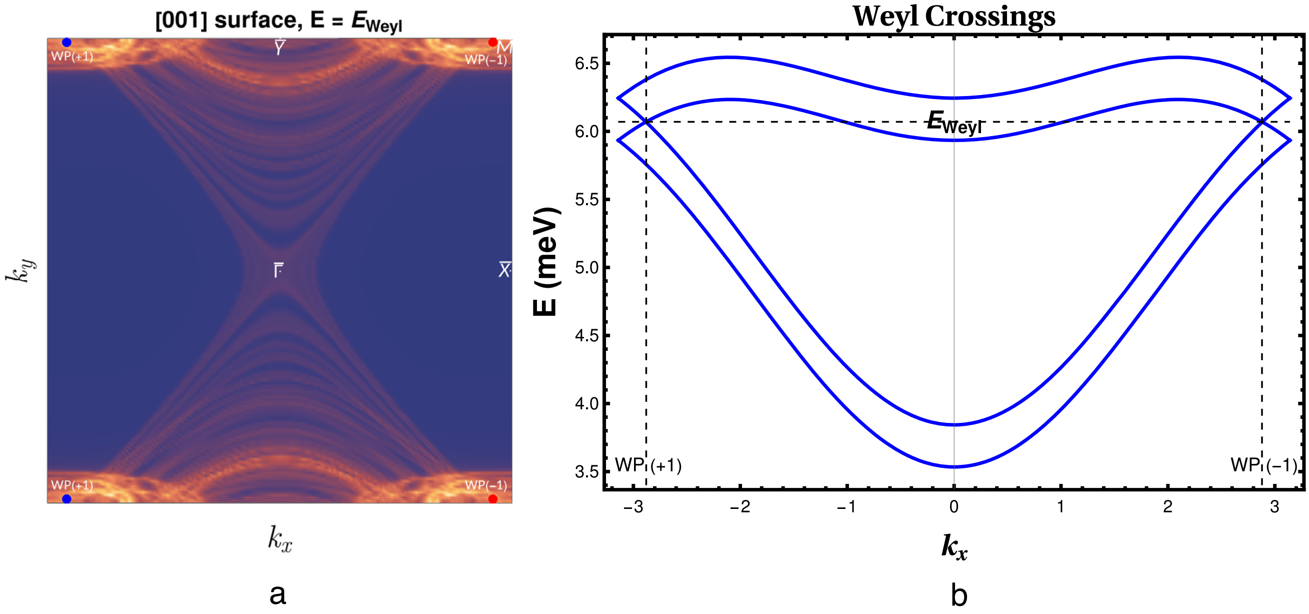

Fig. 3 | Weyl magnons in NdMnO$_3$. a Surface spectral density of magnons in NdMnO$_3$, in a semi-infinite system along the *c*-axis as a function of (k_x, k_y). Red and blue points refer to the projections of the bulk Weyl points over the surface Brillouin zone with topological charges −1 and +1, respectively. As shown in Supplementary Fig. 3, as the iso-energy cut approaches the Weyl energy, magnon arcs start to appear and eventually connect each projection of a Weyl point to the projection of its inversion-related Weyl partner. The intersection of the two magnon arcs forms an X-shaped connectivity pattern that disappears as the iso-energy cut deviates from the Weyl energy. **b** Weyl points in the magnon spectrum of NdMnO$_3$ between the middle two bulk bands. This is plotted on a line connecting two Weyl points with ($k_y = 3.117, k_z = 0$). These two Weyl points are related by two-fold screw $\{2_{100}|\frac{1}{2}\frac{1}{2}\frac{1}{2}\}'$.

applying a magnetic field along the *a*-axis, the $\mathcal{MSG}$ is broken down into the subgroup $P2_1'/c'$, which can also be achieved using a uniaxial strain perpendicular to the [001] direction. This perturbation results in the decomposition of the little groups *irreps* of the $Pn'ma'$ $\mathcal{MSG}$ into *irreps* of the $P2_1'/c'$ subgroup as detailed in Supplementary Section 2. Accordingly, the four-dimensional *irreps* of the original $\mathcal{MSG}$ at the $\mathcal{R}$, $\mathcal{S}$ points decompose into two two-dimensional *irreps* of the magnetic subgroup $P2_1'/c'$, therefore inducing a band gap in the magnon spectrum.

To illustrate the guaranteed topological magnons in our materials search predictions, we explicitly construct a symmetric spin model for this material based on couplings up to third nearest neighbors (see Supplementary Section 2). These values were chosen such that in the classical ground state of the Hamiltonian, ordered moments align along the experimentally-reported ground-state directions[35] shown in Supplementary Fig. 2a. By performing a linear spinwave calculation around that ground state, the magnon band structure is obtained (see Supplementary Fig. 2b). Now, we apply a small magnetic field, 3 T, along the *a*-axis to achieve the symmetry breaking into the $P2_1'/c'$ magnetic subgroup. Upon turning the field on, a gap opens between the first and second pair of magnon bands at the High-Symmetry Points ($\mathcal{HSP}s$) of the BZ. This allows us to calculate the $\mathcal{SI}$ of the induced band gap, using the subgroup $P2_1'/c'$ $\mathcal{SI}$ group $\mathbb{Z}_2 \times \mathbb{Z}_4$ which can be calculated as a function of the *irreps* of the *maximal* **k**-points:

$$z_1 = n^{\Gamma_1^+} \bmod 2 \tag{3}$$

$$z_2 = 2n^{D_1^+D_1^+} + 2n^{E_1^+E_1^+} + n^{\Gamma_1^+} + 3n^{Y_1^+} \bmod 4 \tag{4}$$

which we calculate using *irreps* of the perturbed spectrum (shown in Supplementary Fig. 2d) to be 03 signaling Weyl points pinned to the high-symmetry plane $k_z = 0$. This $\mathcal{SI}$ matches our automated search predictions (see Supplementary Section 76.1) for a nontrivial topology associated with the magnon spectrum gap.

In fact, any spin model, as long as it respects the space group symmetries and hosts the actual magnetic order in the ground state, will always feature an odd $\mathbb{Z}_4$ index after being broken into the $P2_1'/c'$ subgroup. It turns out, as tabulated in the Supplementary Materials, that many other magnetic materials with different magnetic structures also have such an odd $\mathbb{Z}_4$ inversion index in their symmetry indicators. For example, $\mathcal{MSG}$ P_c4_2/ncm & $\mathcal{WP}$ 4*b* has 16 materials that are guaranteed to host symmetry-indicated Weyl magnons, if broken down to the subgroup $C2'/c'$ (15.89) through suitable perturbations. The same conclusion applies to 3 materials belonging to the $\mathcal{MSG}$ P_cmna & $\mathcal{WP}$ 4*a* after being broken down to the $P2_1'/c'$ subgroup. Here, we find two pairs of Weyl magnons around $E = E_{Weyl}$~6.07 meV pinned to the $k_z = 0$ plane. One Weyl point is located at momentum (2.882, 3.117, 0) with − 1 topological charge. Other Weyl points are related to this one by symmetries as follows. After applying the field (along [100]), only two-fold screw $\{2_{100}|\frac{1}{2}\frac{1}{2}\frac{1}{2}\}'$, glide $\{m_{100}|\frac{1}{2}\frac{1}{2}\frac{1}{2}\}'$ (where $'$ means combined with time reversal) and inversion $\mathcal{I}$ survive. The bulk Weyl points (see Fig. 3b and Supplementary Fig. 2c) are related as follows:

- $\mathcal{I}$ relates points (k_x, k_y, k_z) to $(-k_x, -k_y, -k_z)$, with opposite chirality.
- $\{2_{100}|\frac{1}{2}\frac{1}{2}\frac{1}{2}\}'$ relates (k_x, k_y, k_z) to $(k_x, -k_y, -k_z)$, with the same chirality.

The topological charge of the Weyl points was calculated as the Chern number of the upper two bands on a small sphere enclosing the Weyl point using the method developed by[37] and the fermionic dual of the magnon Hamiltonian[38]. To compute the surface states, we consider a semi-infinite system along the *c*-axis and calculate the surface spectral density $N_s(E, k_x, k_y)$ using the Green's function renormalization technique[39]:

$$N_s(E, \boldsymbol{k}) = -\frac{1}{\pi} \lim_{\eta \to 0^+} \mathrm{Im}\mathrm{Tr}\, G_{00}(E + \mathrm{i}\eta, \boldsymbol{k}) \tag{5}$$

where G_{00} is the block of the Green's function that corresponds to the principal layer containing the surface[39]. In Fig. 3a and Supplementary Fig. 3, one can see that each pair of Weyl magnons is connected by a surface magnon arc, analogous to Fermi arcs in Weyl semimetals. This results in a total of two magnon arcs due to the symmetry-related bulk Weyl magnons discussed earlier. The sequence of the iso-energy cuts for the surface spectral

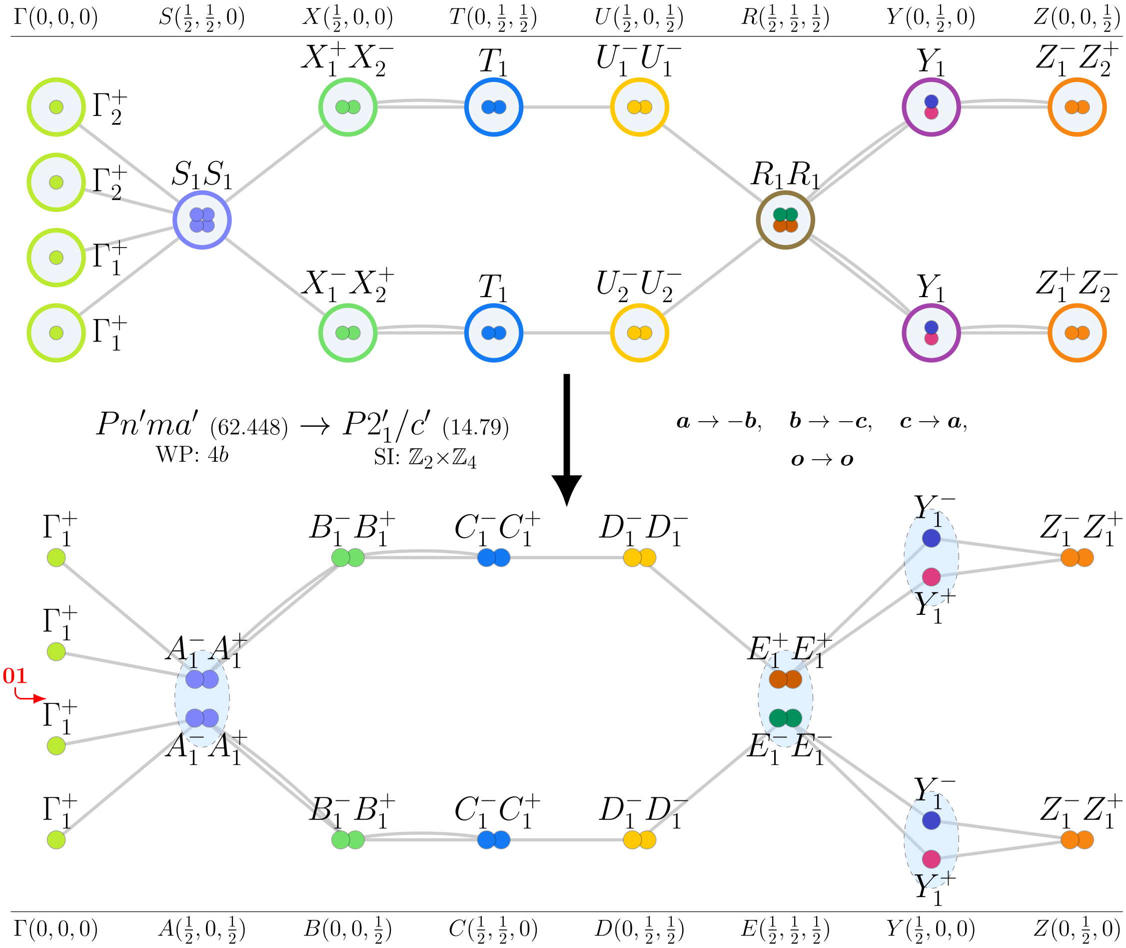

Fig. 4 | Schematic representation of the magnon band structure in NdMnO$_3$. Upon the symmetry breaking discussed in the main text, the resulting order of the *irreps* at the $\mathcal{HSPs}$ is not unique. This is one possibility that the band structure might fall into. Unlike the constructed spin model that produced a 03 $\mathcal{SI}$, a different spin model can give rise to a different possibility, such as the one presented here, in which the $\mathcal{SI}$ is 03. Regardless of the spin Hamiltonian details, the $\mathcal{SI}$ belongs to the same topological class.

density, in Supplementary Fig. 3, enables a clear distinction between bulk and surface states. At energies below and above the Weyl node energy, the spectral weight is characterized by diffuse features, indicative of bulk band projections. In contrast, while approaching the Weyl energy, a sharply defined X-shaped pattern emerges, consisting of arc-like features that connect the projections of Weyl nodes. Another possible arrangement of *irreps* is shown in Fig. 4, in which *irreps* of *D* point are swapped compared to Supplementary Fig. 2b, resulting in a band gap with a $\mathcal{SI}$ value of 01, which belongs to the same topological class.

Ca$_2$RuO$_4$

Now we discuss another example for which preliminary INS data exist in the literature[40]. Ca$_2$RuO$_4$ is a Mott insulator that undergoes an antiferromagnetic ordering transition at $T_N = 110$ K[41]. It turns out that Ca$_2$RuO$_4$ has a rich phase diagram due to the interplay between spin, charge, orbital, and lattice degrees of freedom[42], however, here we will focus on the spin excitations around its AFM ground state reported in ref. 41. In this magnetically ordered phase, the magnetic moments of the Ru^{4+} ions align mostly along the orthorhombic *b* axis with a $\overrightarrow{Q}=0$ propagation vector. It was also shown recently[41] that the magnetic moments have a canting angle from the c-axis. This magnetically ordered structure is such that the moments are located at the $\mathcal{WP}$ 4*a* of $\mathcal{MSG}$ *Pbca* (61.433), as shown in Supplementary Fig. 4. These inputs indicate symmetry-enforced two-fold degeneracy at all high-symmetry points ($\mathcal{HSPs}$) except at *Γ*.

According to our tabulated results (see Supplementary Section 71), this structure will feature at least one induced topological gap upon lowering the symmetry group down to the $P\bar{1}$ (2.4) subgroup. This subgroup has only inversion symmetry, which can be realized by applying a magnetic field in a low-symmetry direction that breaks all $\mathcal{MSG}$ symmetries but inversion. Unlike the previous example, here we perform a linear spin wave (LSW) calculation based on the magnetic interactions reported in the INS study[40], including up to third nearest neighbor intraplane Heisenberg interaction, single-ion anisotropy along the *b* axis, and an antiferromagnetic inter-layer coupling. We also add extra small symmetry-allowed terms to remove accidental degeneracies, by requiring that our LSW spectrum closely matches the lowest pair of bands observed in the INS study at zero field. Our main purpose is to show that upon the specified symmetry breaking, three band gaps are induced with at least one gap admitting nontrivial $\mathcal{SI}$. The LSW spectrum based on our spin model (for more details, see Supplementary Section 2) is shown in Supplementary Fig. 4b where the four Ru^{4+} magnetic sublattices give rise to four magnon bands. The two lower energy modes are very close in energy to the magnons observed in the INS study[40].

By applying a 10 T magnetic field along a low-symmetry direction, we achieve symmetry breaking down to the subgroup $P\bar{1}$ (2.4), which has a $\mathcal{SI}$ group $\mathbb{Z}_2^3\times\mathbb{Z}_4$. In this symmetry-breaking process, all two-dimensional *irreps* decompose into one-dimensional *irreps* of $P\bar{1}$. Therefore, such a perturbation lifts all symmetry-protected degeneracies in both the higher and lower pairs of magnon bands at all $\mathcal{HSPs}$. This gives a total of three band gaps, with the middle gap acquiring a nontrivial inversion $\mathcal{SI}$ *1112*. This value indicates that the Chern number of the two lower (and accordingly the two higher) magnon bands on the $k_i = 0, \pi$ planes (where $i = x, y, z$) is an odd integer, i.e., it is 1 mod 2. This is confirmed by explicit Chern number calculations shown in Supplementary Fig. 5. The $\mathbb{Z}_4 = 2$ index diagnoses difference between the Chern numbers on $k_z = 0$ and $k_z = \pi$ planes, which is confirmed as shown in Supplementary Fig. 5. This signals an even number of Weyl points between the $k_i = 0$, π planes at generic momenta. This is consistent with our spin model that gives 14 Weyl points in half of the 1st BZ $k_i \in (0, \pi)$, with the sum of their topological charges in half of the Brillouin zone equal to 2. The presence of an even number of Weyl points accounts for the even disparity in Chern numbers between the high-symmetry planes. Their opposite-charge partners in $k_i \in (-\pi, 0)$ are related by inversion symmetry. Explicit locations of the Weyl points and their topological charges are summarized in Supplementary Table 2.

The $\mathcal{SI}$ of $P\bar{1}$ can be calculated using parities of magnon Bloch eigenstates at the 8 $\mathcal{HSP}s$ as follows:

$$\begin{aligned} z_{2\mathcal{I},x_i} &= \sum_{\boldsymbol{k}\in \mathrm{HSPs},\, k_{x_i}=\pi} \tfrac{1}{2}\left(N_{\boldsymbol{k}}^{-} - N_{\boldsymbol{k}}^{+}\right) \bmod 2 \\ z_{4\mathcal{I}} &= \sum_{\boldsymbol{k}\in \mathrm{HSPs}} \tfrac{1}{2}\left(N_{\boldsymbol{k}}^{-} - N_{\boldsymbol{k}}^{+}\right) \bmod 4 \end{aligned} \tag{6}$$

where $N_{\boldsymbol{k}}^{\pm}$ is the number of bands with ± inversion eigenvalue below a given gap, and $x_i = \{x, y, z\}$. The spectra for the unperturbed and perturbed LSW Hamiltonian are shown in Supplementary Figure 4b, d, along with the band *irreps* and the calculated values of the $\mathcal{SI}s$ of the band gaps. Note that as long as the *irreps* of the *Pbca* (61.433) decompose into *irreps* of the subgroup $P\bar{1}$ (2.4) via a small perturbation, the $\mathcal{SI}$ of the middle gap is robust with the same value as shown in Supplementary Fig. 4d. This is regardless of the form of the symmetry-allowed spin model or the external perturbation chosen to break the symmetry. The $\mathcal{SI}$ for other two band gaps depends on the spin model and the used perturbation. For example, a different spin model can lead to a different arrangement of *irreps* (see Supplementary Fig. 6) that has only one nontrivial $\mathcal{SI}$ in the middle gap. Although the focus so far was on the middle gap due to its robust $\mathcal{SI}$, according to our calculation of the LSW spectrum, the first and third band gaps also exhibit nontrivial topology in the perturbed spin Hamiltonian reported in the INS study[40]. However, the sizes of these gaps are smaller, at least in our spin model, compared to the middle gap. Overall, all calculated values of $\mathcal{SI}s$ are consistent with our automated search results in Supplementary Section 71.

Experimental accessibility of candidates

The experimental confirmation of the predicted topological magnons in this work often requires the application of mechanical strains and/or magnetic/electric fields in controlled directions. This requires the growth of thin films and crystals of macroscopic dimensions to realize these effects. Synthetic routes to these high-quality and macroscopic-sized crystals of many of the identified families of materials have been well established in the literature, and for which a few demonstrative examples will be provided here. In the case of transition metal insulators, single crystals of $NiFe_2O_4$ have been grown at up to the cm scale by Czochralski growth using a Na_2CO_3 flux[43]. Meanwhile, doping of MnV_2O_4 has been achieved using Cr and Zn to adjust the p-type doping and modulate the magnetic transition temperature[44]. High-quality crystals of the metal-to-insulator transition compound NiS_2 have been grown at the multiple mm scale by both Te flux and chemical vapor transport growths[45,46]. Thin films of perovskite candidate $BiCrO_3$ have been grown on many different substrates, including $SrTiO_3$ (001) and $NdGdO_3$ (110), allowing for control of strains applied from the substrate[47]. *f*-block insulator DyOCl is a 2D material and has been grown at the mm scale and exfoliated, allowing for similar substrate control for measurement[48]. Inter-metallic Mn_5Si_3 growth has been demonstrated as both mm-sized single crystals and as thin films grown on Si (111)[49,50]. Additionally, large single crystals of $NdMnO_3$, highlighted in the "Topological magnon compounds" section, have been grown by a floating zone growth in air[51]. For Ca_2RuO_4, single crystals of multi-millimeter size have been grown via floating growth using Ruthenium self-flux and an Ar/O_2 atmosphere to precisely control the oxygen concentration[52]. Further tuning of the structure of Ca_2RuO_4 can be obtained by alloying Sr in both powders and single-crystal form. We list some interesting candidate materials that host either gapless Weyl states or magnon axion insulating states upon the relevant perturbations detailed in the Supplementary Materials, alongside their chemical categories in Table 1.

Discussion

In this work, we present a major development in the symmetry-based approach for identifying topological magnons through a fully automated algorithm that enables an efficient, large-scale search for candidate materials hosting field-induced topological magnons. This innovation significantly broadens the scope of materials exploration, surpassing the limitations of manual or limited methods. It provides a powerful tool for uncovering novel topological phases in magnetic systems, opening new avenues for exploration in this area. Applying this algorithm to all 1649 magnetic materials in BCS with a commensurate magnetic order, we ran a large-scale search and discovered 387 candidate materials for topological magnons. We further discussed examples and experimental accessibility of these candidate materials. It is noteworthy that some of materials identified in this work can admit a complex magnetic phase diagram where spin reorientation can occur, resulting in a different magnetic structure, for example upon cooling (e.g., the Morin transition in α-Fe_2O_3[53] and the abrupt spin reorientation transition in $CeFeO_3$[54] at $T = 240$ K), under pressure (e.g., $FeBO_3$[55]), or under doping (e.g., $SmFeO_3$[56]). Therefore, our results are valid for each material if it belongs to the magnetic phase reported on BCS and detailed in the Supplementary Materials.

Now we discuss the limitations of our findings. Firstly, we note that the perturbations we consider for inducing topological band gaps (electric, magnetic fields, and mechanical strains) should be small enough so that upon symmetry reduction, the *irreps* splitting does not swap the order of the subgroup *irreps* at any momentum $\boldsymbol{k}$ with other subgroup *irrep*s. The strength of the required perturbation will quantitatively depend on the energetic details of the considered magnet and, therefore, on the interaction strengths. For example, for the case of applying mechanical strains, distortion of the lattice geometry and the magnetic structure[57–59], implicitly encoded in the $\mathcal{MSG}$ reduction to one of its subgroups, can strongly affect the exchange integrals t between orbitals at neighboring lattice sites, usually mediated by the super-exchange mechanism, consequently affecting the exchange couplings J~t^2/u, where u is the on-site Hubbard repulsion. Therefore, energetically, to a leading order, strain amounts to changes in the spin–spin exchange interactions[21,57,58], subject to the symmetry constraints of the strain-induced lattice structure.

Another limitation is the neglect of finite-temperature effects and magnon–magnon interactions, which lead to magnon lifetime broadening that can obscure the induced magnon band gap[60–64] that protects the topology. In realistic materials, the magnon–magnon interaction will depend on the spin value S of the magnetic moments (higher S indicates the suppression of the magnon–magnon interaction terms as seen in Eq. (13), at least at small finite temperatures compared to the transition temperature) and the exchange couplings between the magnetic moments. However, we expect that the topological magnons discovered in this work survive when the perturbation-induced magnon band gap is much larger than the broadening.

Additionally, the experimental detection of such symmetry-indicated topological features (e.g., Weyl nodes or band gap opening) can be challenging depending on the energetics of the magnon spectrum, the anticipated topology, and the accessibility to apply a sufficiently large perturbation. Remarkably, INS (with a typical energy resolution of ~1–2 meV) has been successful so far not only in mapping the magnon dispersion and intensity across the full BZ, but also in accessing topological features such as band gap openings and band crossings (e.g., Dirac nodes) through characteristic intensity modulations[60,65,66]. Additionally, indirect signatures for the nontrivial magnon band topology can be seen in the thermal Hall effect of magnons[67–69]. However, in cases where interesting topological features appear at small energy scales (a few meV), it can be difficult for techniques such as RIXS and SPEELS with typical energy

Table 1 | Chemical categories of some synthesis-*relevant* topological magnon compounds identified in this work with a nontrivial $\mathbb{Z}_4$ inversion index upon breaking into one of the magnetic subgroups (*e.g.* $P\bar{1}$, $P2_1'/c'$, $C2'/m'$, $C2'/c'$, ..*etc*) of their respective $\mathcal{MSG}s$

Category	Properties	Materials
I- Transition metal magnets		
I-A	Transition metal insulators	α-Fe_2O_3†, CoO, $MnTe_2$, $NiFe_2O_4$, $NiCr_2O_4$, MnV_2O_4, $CdYb_2S_4$, $CdYb_2Se_4$, $MnPb_4Sb_6S_{14}$, $FePb_4Sb_6S_{14}$, $Ba_2CoO_2Ag_2Se_2$, $Sr_2CoO_2Ag_2Se_2$, $Sr_2Fe_3S_2O_3$, BaCoSO, Sr_3ZnIrO_6, Ca_4IrO_6, Ca_3LiRuO_6, Sr_3LiRuO_6, Sr_3NaRuO_6, $SrFeO_2$, Ca_3LiOsO_6, Ca_2MnGaO_5, $CuSb_2O_6$, Cr_2ReO_6, $Ca_2Fe_2O_5$, Mn_3TeO_6, $FeTa_2O_6$, $GeNi_2O_4$, LiMnAs, CsMnP, CsMnBi, RbMnAs, RbMn, RbMnP, KMnP, KMnAs, RbMnAs, RbMnBi
I-B	Metallic TM pnictogens and chalcogens	CrN, $Li_{0.5}FeCr_{1.5}S_4$, $FeCr_2S_4$, $SrMnSb_2$, $CoNb_3S_6$, $CsCo_2Se_2$, $CaCo_{1.86}As_2$, $Sr_2Cr_3As_2O_2$, $CuSe_2O_5$
I-C	Metal-to-insulator transition compounds	NiS_2, $KCuMnS_2$, USb
I-D	Transition metal intermetallics	$MnPt_{0.5}Pd_{0.5}$, Mn_3Pt, MnCoGe, Mn_5Si_3, $Fe_{0.7}Mn_{0.3}$, $Ni_{1.64}Co_{0.36}Mn_{1.28}Ga_{0.72}$, Mn_3Sn_2, $PrMnSi_2$, $CaFe_4Al_8$, FeGe, FeSn, $FeSn_2$, $FeGe_2$, $Mn_3Cu_{0.5}Ge_{0.5}N$, Mn_3GaN, Mn_3ZnN, Mn_3GaC, Mn_3CuN, Mn_2As, Fe_2As, Cr_2As, $EuFe_2As_2$
II- f-block magnets		
II-A	Insulating f-block magnets	UO_2, NpSe, NpS, DyOCl, HoP, La_3OsO_7, $La_{2.8}Ca_{0.2}OsO_7$, $Cd_2Os_2O_7$, $Ho_2Ru_2O_7$, $Er_2Ru_2O_7$, $Dy_3Al_5O_{12}$, $Tb_3Al_5O_{12}$, $Ho_3Al_5O_{12}$, $Er_3Ga_5O_{12}$, $Dy_3Ga_5O_{12}$, $Tb_3Ga_5O_{12}$, $Ho_3Ga_5O_{12}$, $Ln_3Tr_5O_{12}$, $Tm_2Mn_2O_7$, Ho_2CrSbO_7, $Ho_2Ru_2O_7$, $Er_2Ti_2O_7$, $Gd_2Sn_2O_7$, $Er_2Pt_2O_7$, $Er_2Sn_2O_7$, $Gd_2Ti_2O_7$, $Nd_2Sn_2O_7$, $Nd_2Hf_2O_7$, $Nd_2Zr_2O_7$, Nd_2ScNbO_7, $Sm_2Ti_2O_7$, $Tb_2Sn_2O_7$, $Yb_2Ti_2O_7$, $Yb_2Sn_2O_7$
II-B	Metallic f-block pnictogens and chalcogens	UP, USb_2, UP_2, UGeS, UGeTe, NpBi, NpTe, NdCoAsO, LaCrAsO, $CeCo_2P_2$, CeSbTe
II-C	f-block Intermetallics	$Ho(Co_{0.66}Ga_{0.33})_2$, $CeIr(In_{0.97}Cd_{0.03})_5$, ErNiGe, $NdCo_2$, GdMg, Pr_2Pd_2In, NdZn, Ho_3NiGe_2, Pr_3CoGe_2, $Tb_{0.6}Y_{0.4}RhIn_5$, NdMg, NdPt, $TbPd_{2.05}Sn_{0.95}$, Ho_3Ge_4, $NdNiMg_{15}$, Er_3Ge_4, $Ce_2Ni_3Ge_5$, HoRh, $Yb_2Pd(In_{0.4}Sn_{0.6})$, $NdPd_5Al_2$, $ErFe_2Si_2$, $NdScSiC_{0.5}H_{0.2}$, $UNiGa_5$, UPd_2Ge_2, URh_3Si_5, $NpNiGa_5$, $U_2Pd_{2.35}Sn_{0.65}$, $ErMn_2Ge_2$, YMn_2Si_2, YMn_2Ge_2, $EuMn_2Si_2$, $CeMn_2Si_2$, $NdMn_2Si_2$, $CeMn_2Si_2$, $PrMn_2Si_2$, $PrMn_2Si_2$, $ErMn_2Ge_2$, $ErMn_2Si_2$, $TbMn_2Si_2$, DyCu, TbPt, $TbPt_{0.8}Cu_{0.2}$, NdSi, DyPt, TmNi, PrSi, $NdNi_{0.6}Cu_{0.4}$, HoNi, HoPt, ErPt, TmPt, Tb_2CoGa_8, Dy_2CoGa_8, Nd_2RhIn_8, U_2Rh_2Sn, U_2Ni_2Sn, $CeRh_2Si_2$, $CeRu_2Al_{10}$, U_2Ni_2In, $YbCo_2Si_2$
III- Structurally distinct magnets		
III-A	Perovskite oxides and their derivatives	$BiCrO_3$, $TbCr_{0.5}Mn_{0.5}O_3$, $Lu_{0.6}Mn_{0.4}MnO_3$, $Pb_{0.7}Bi_{0.3}Fe_{0.762}W_{0.231}O_3$, $Pb_{0.8}Bi_{0.2}Fe_{0.728}W_{0.264}O_3$, Nd_2CuO_4, Sr_2IrO_4, Nd_2NiO_4, Ca_2RuO_4, La_2NiO_4, $LaSr_3Fe_3O_9$, $CaCu_3Fe_2Sb_2O_{12}$, Sr_2CoOsO_6, Sr_2FeOsO_6, $Cu_3Ni_2SbO_6$, Bi_2RuMnO_7, $NdFeO_3$, $CeFeO_3$†, $TbFeO_3$, $SmFeO_3$†, $NaOsO_3$, $LaCrO_3$, $YCrO_3$, $LaMnO_3$, $ErCrO_3$, $TmCrO_3$, $YRuO_3$, $PrMnO_3$, $Pr_{0.95}K_{0.05}MnO_3$, $NdMnO_3$, $KMnF_3$, $NdMnO_3$, $(CH_3NH_3)(Co(COOH)_3)$, $Ho_{0.2}Bi_{0.8}FeO_3$, $Ho_{0.15}Bi_{0.85}FeO_3$, $La_{0.875}Ba_{0.125}Mn_{0.875}Ti_{0.125}O_3$, $La_{0.90}Ba_{0.10}Mn_{0.90}Ti_{0.10}O_3$, $La_{0.95}Ba_{0.05}Mn_{0.95}Ti_{0.05}O_3$, $La_{0.95}Ba_{0.05}MnO_3$, $LaMnO_3$, $YCr_{0.5}Mn_{0.5}O_3$, $SmFeO_3$, $SrRuO_3$, $TbCrO_3$, $DyCrO_3$, $TeNiO_3$, YVO_3, $LaSrFeO_4$, Nd_2CuO_4, Pr_2CuO_4, $LaSrFeO_4$, $LaCaFeO_4$, $LaBaFeO_4$, $La_{0.75}Bi_{0.25}Fe_{0.5}Cr_{0.5}O_3$, $LaCrO_3$, $CeFeO_3$, $InCrO_3$, $TlCrO_3$, $ScCrO_3$, La_2NiO_4, Nd_2NiO_4, La_2CoO_4, Gd_2CuO_4, Sm_2CuO_4, Eu_2CuO_4, $Bi_{0.8}La_{0.2}Fe_{0.5}Mn_{0.5}O_3$, $PrCrO_3$, $SmCrO_3$, $NdMn_{0.8}Fe_{0.2}O_3$, $Bi_{0.8}La_{0.2}Fe_{0.5}Mn_{0.5}O_3$, $PrCrO_3$, $SmCrO_3$, $NdMn_{0.8}Fe_{0.2}O_3$, $Rb_2Fe_2O(AsO_4)_2$, $NdMnO_3$, $NdMn_{0.8}Fe_{0.2}O_3$, $Pr_{0.5}Sr_{0.5}CoO_3$, $Pr_{0.5}Sr_{0.4}Ba_{0.1}CoO_3$, $Pr_{0.5}Sr_{0.5}MnO_3$, $(Tm_{0.7}Mn_{0.3})MnO_3$, $(Ho_{0.8}Mn_{0.2})MnO_3$, $Tb_{0.55}Sr_{0.45}MnO_3$, $Tb_{0.55}Sr_{0.45}MnO_3$, $SmCrO_3$, $TbFeO_3$, Sc_2NiMnO_6, La_2CoPtO_6, $Ca_2Fe_{0.875}Cr_{0.125}GaO_5$
III-B	Halides and oxyhalides	$KNiF_3$, $KMnF_3$, FeF_3, $LiCoF_4$, $NaMnF_4$, Na_2NiFeF_7, $CsMn_2F_6$, $Fe_2F_5(H_2O)_2$, Cr_2F_5, $CsMnF_4$, $TlMnF_4$, Na_2NiCrF_7, $CsCoCl_3(D_2O)_2$, $CsNiF_3$, $SrFeO_2F$, $La_2NiO_3F_2$, $La_{0.5}Sr_{0.5}FeO_{0.5}F_{0.5}$, $Mn_2SeO_3F_2$, $Cu_3Mg(OD)_6Br_2$, $La_2NiO_3F_{1.93}$
III-C	Polyatomic oxides (sulfates, phosphates, carbonates, vanadates, germanates, and silicates)	$NiSO_4$, $FeSO_4$, $CoSO_4$, $FeSO_4F$, $FeOHSO_4$, $Li_2Fe(SO_4)_2$, $NaFeSO_4F$, $NaCoSO_4F$, $Co_3(PO_4)_2$, $CuFe_2(P_2O_7)_2$, Fe_2MnBO_5, $AgMnVO_4$, VPO_4, $Na_3Co(CO_3)_2Cl$, $Na_2BaMn(VO_4)_2$, $MnCO_3$, $NiCO_3$, $CoCO_3$, $Cu_3Y(SeO_3)_2O_2Cl$, $Cu_3Bi(SeO_3)_2O_2Br$, $(NH_2(CH_3)_2)(FeMn(HCOO)_6)$, $(CH_3NH_3)Co(COOH)_3$, $(NH_2(CH_3)_2)(FeCo(HCOO)_6)$, $NH_4FeCl_2(HCOO)$, $[C(ND_2)_3]Mn(DCOO)_3$, $KFe_3(SO_4)_2(OH)_6$, $NaFe_3(SO_4)_2(OH)_6$, $AgFe_3(SO_4)_2(OD)_6$, $FeBO_3$†, $CoFePO_5$, $NaFePO_4$, $Na_2BaFe(VO_4)_2$, $LaMn_3V_4O_{12}$, $ZrCo_2Ge_4O_{12}$, $CeCo_2Ge_4O_{12}$, $CeMnCoGe_4O_{12}$, $ZrMn_2Ge_4O_{12}$, $GdFeZnGe_4O_{12}$, $ErFeCuGe_4O_{12}$, $NaCeGe_2O_6$, $Fe_4Si_2Sn_7O_{16}$, Mn_2SiO_4, Mn_2GeO_4, $CuCl(C_4H_4N_2)_2(BF_4)$, $CuBr(C_4H_4N_2)_2(BF_4)$

Such values diagnose either gapless Weyl magnons or gapped magnon axion insulator states depending on the $\mathcal{MSG}$ of the chosen material and possibly the details of the magnetic interactions between spins therein. † highlights some materials that admit spin reorientation transitions as mentioned in the "Discussion" section. For the full table of materials that passed our search filters, see Supplementary Section 1.

resolutions of ~30–100 meV and ~10–20 meV, respectively, although sensitive to spin excitations.

Furthermore, while the nontrivial topology of magnon bands ensures robustness[70,71], against certain classes of disorder, particularly static and elastic impurities that preserve magnon energy, this protection is not absolute; in realistic materials, dynamic defects such as thermally excited phonons[72,73], time-dependent spin disorder, or fluctuating local lattice deformations can act as energy sinks, giving rise to inelastic scattering processes. These interactions not only compromise magnon coherence and lifetime but may also induce transitions out of the topological magnonic states, thereby weakening the topological protection. A comprehensive understanding of magnon transport thus requires considering both elastic and inelastic scattering channels, especially in finite-temperature regimes where dynamic processes are prevalent. A possible resolution to overcome such effects might be the theoretical proposal by Malz et al.[74] to enhance the effects of topology of magnon band structures using an electromagnetic field to pump more magnons (via magnon-photon coupling) into the topology-relevant states (e.g., states with large Berry curvature in the case of insulating magnon band structure or states close to Weyl nodes in the case of semi-metallic magnon spectra) to drive large non-equilibrium steady state magnon edge currents.

In the symmetry-based search algorithm discussed in this work, spin-orbit couplings (SOCs) are assumed in all magnetic materials, which explicitly break the $SO(3)$ spin rotational symmetries. Magnets of negligible (or weak) SOCs can exhibit distinct properties compared to spin-orbit-coupled ones discussed in this work, such as different topological properties[75], and different representations associated with spin-group symmetries in the case of negligible SOC[76–79]. New physical phenomena can emerge in magnets with negligible SOCs, such as recently discovered altermagnetism in collinear magnets[79–81]. One future direction is to extend the current search algorithm to altermagnets with weak SOCs, making use of the representation theory of spin space groups. This can lead to new types of topological magnons in altermagnetic materials, protected by spin-group symmetries.

Another future direction is to generalize the current approach to magnon polarons, which arise from the hybridization of magnons and phonons in magnetically ordered materials. It is well established that this hybridization can lead to the emergence of topological magnon polarons[82–84]; however, only a few materials have been identified to host these topological bosonic modes[85]. The current theoretical framework can be expanded to encompass not only pure topological magnons[21] and topological phonons[11], but also to enable a systematic search for materials hosting topological magnon polarons. These intriguing possibilities open the door to future research directions, which we aim to explore in upcoming projects.

Methods

Review of topological quantum chemistry

In this work, we are interested in crystalline solids with a commensurate long-range magnetic order formed by localized magnetic moments that is described by a local order parameter $\langle S_i^\alpha \rangle$ where i is the lattice site index and α is the component of spin $\overrightarrow{S}_i$. A general bilinear spin Hamiltonian that captures the interactions between the localized moments takes the following form:

$$\hat{\mathcal{H}} = \frac{1}{2} \sum_{i,j;a,b;\alpha,\beta} J_{ia,jb}^{\alpha,\beta} \hat{S}_{i,a}^{\alpha} \hat{S}_{j,b}^{\beta} - g\mu_B \sum_{i,a;\alpha} B^{\alpha} \hat{S}_{i;a}^{\alpha} \tag{7}$$

where i, j run over the primitive magnetic cells, a, b run over the magnetic sublattices, and α, β run over the spin components. Such a Hamiltonian can describe exchange interactions, single-ion anisotropy, and couplings to an external magnetic field. The magnetic order breaks the time reversal and space group $\boldsymbol{G}_H$ symmetry of this Hamiltonian down to a magnetic space group $\boldsymbol{G}_M$, whose elements leave the ordered magnetic moments $\langle S_i^\alpha \rangle$ invariant; therefore, $\boldsymbol{G}_M$ is the relevant symmetry group for magnon bands. Here, we restrict our attention to spin-orbit-coupled magnets where spin rotational symmetries are absent. This makes the relevant magnetic space groups for magnons *single-valued* due to the bosonic nature of the excitations.

Spinwave excitations arise from the transverse fluctuations around the ordered moments, and they give rise to a spectrum of dispersive, coherently propagating magnons, which is the focus of this study. In the framework of topological quantum chemistry (TQC)[24,26,27,86], the band representations[87] can be constructed based on three symmetry ingredients: the space group ($\mathcal{SG}$) of the lattice, the Wyckoff positions ($\mathcal{WP}$), and the nature of the atomic orbitals in the material[2426]. The band representation of the space group ($\mathcal{SG}$) is obtained by inducing the representation of the site symmetry group $\mathcal{SSG}$ of the $\mathcal{WP}$ to the full space group of the lattice:

$$\rho_G = \rho \uparrow G \tag{8}$$

where ρ is a representation of the $\mathcal{SSG}$ which is related to the full space group through the coset decomposition:

$$G = \cup_\alpha g_\alpha G_{\boldsymbol{q}} \tag{9}$$

where $G_{\boldsymbol{q}}$ is the $\mathcal{SSG}$ of the $\mathcal{WP}$s $\mathbf{q}$ of interest, and g_α are the coset representatives of $G_{\boldsymbol{q}}$ which map the points $\boldsymbol{q}$ to other points of the $\mathcal{WP}$. Then this band representation is reduced to the representation of the little co-groups of the points of interest in the BZ, usually high-symmetry momenta:

$$(\rho \uparrow G) \downarrow G_K \approx \rho_{G_K} \tag{10}$$

where G_K is the little group of the momentum K of interest. In analogy, to build a magnon band representation[88], we start with building a representation of the magnetic $\mathcal{SSG}$ $\boldsymbol{G}_{\boldsymbol{q}_1}$ where $\boldsymbol{q}_1$ belongs to the Wyckoff position of the magnetic moments, which is a subgroup of $\boldsymbol{G}_M$ that leaves both the site (up to a primitive lattice translation) and the magnetic order invariant. This translates into the requirement that $\boldsymbol{S}^z$ transforms trivially under elements of $\boldsymbol{G}_{\boldsymbol{q}_1}$:

$$g_i \boldsymbol{S}_{\boldsymbol{q}_1}^z = \boldsymbol{S}_{\boldsymbol{q}_1}^z \;\; \forall g_i \in \boldsymbol{G}_{\boldsymbol{q}_1} \tag{11}$$

where z refers to the local orientation of the magnetic moment. This reduces the number of allowed magnetic $\mathcal{SSG}$s to 31 magnetic point groups that preserve the magnetic order out of the 122 magnetic point groups[88]. Since magnons are transverse modes constructed from the $\hat{S}^{\pm}$ components, the allowed representations of the 31 magnetic point groups compatible with the magnetic order are determined by how the transverse spin components transform under $\mathcal{SSG}$. The magnetic $\mathcal{SSG}s$ compatible with the magnetic order along with the induced pair of elementary band representations (reflecting the particle-hole symmetry of the spin wave Hamiltonian), were worked out and tabulated[88]. The band co-representations induced from a chosen $\mathcal{WP}$ of a $\mathcal{MSG}$ have been worked out[8,25] and accessible via the BCS tool MBANDREP[8,25]. Here, we work directly with the representations of the full magnetic space group ($\mathcal{MSG}$) rather than starting with the little co-groups' *irreps* at individual k-points. In particular, we employ the framework of magnetic band representations, as implemented in the BCS tool MBANDREP[8,25], which correctly handles the induction of $\mathcal{MSG}$ representations, from representations of the magnetic $\mathcal{SSG}$s of the magnetic $\mathcal{WP}s$. These induced $\mathcal{MSG}$ co-representations are subsequently restricted to high-symmetry momenta in the Brillouin zone (BZ) to extract the relevant *irrep* labels of the magnon bands, forming the key input to our topological classification methodology summarized in Fig. 2.

Linear spin wave theory

For a generic bilinear spin Hamiltonian,

$$\hat{\mathcal{H}} = \frac{1}{2} \sum_{i,j;a,b;\alpha,\beta} J_{ia,jb}^{\alpha,\beta} \hat{S}_{i,a}^{\alpha} \hat{S}_{j,b}^{\beta} \tag{12}$$

the standard method for calculating the spinwave excitations is linear spin wave theory, which relies on an expansion in the spin fluctuations around the classical ground-state order. In LSWT, transverse spin components are transformed to magnon creation $\hat{a}^\dagger$ and annihilation operators $\hat{a}$ using the *Holestein–Primakoff* transformation:

$$\begin{aligned} \hat{S}^z &= S - \hat{a}^\dagger \hat{a} \\ \hat{S}^+ &= \sqrt{2S}\sqrt{1 - \tfrac{\hat{a}^\dagger \hat{a}}{2S}}\hat{a} = \sqrt{2S}\left(1 - \tfrac{\hat{a}^\dagger \hat{a}}{4S}\right)\hat{a} + \ldots \\ \hat{S}^- &= \sqrt{2S}\hat{a}^\dagger \sqrt{1 - \tfrac{\hat{a}^\dagger \hat{a}}{2S}} = \sqrt{2S}\hat{a}^\dagger \left(1 - \tfrac{\hat{a}^\dagger \hat{a}}{4S}\right) + \ldots \end{aligned} \tag{13}$$

with the magnon operators satisfy the bosonic commutation relations $\left[\hat{a}_i, \hat{a}_j^\dagger\right] = \delta_{ij}$ and $\left[\hat{a}_i, \hat{a}_j\right] = \left[\hat{a}_i^\dagger, \hat{a}_j^\dagger\right] = 0$. ($S^x$, S^y) are the transverse spin components are in its local frame, that is, locally rotated such that the z-axis is aligned along the polarization direction $\langle \boldsymbol{S}_i \rangle = S_i \hat{z}_i = (0, 0, S_i)$. The square root is expanded in powers of $\frac{1}{S}$ and by truncating it to a linear order in $\frac{1}{S}$, a Hamiltonian of the form:

$$\hat{H}_{SW} = \hat{H}^{(0)} + \hat{H}^{(2)} + \hat{H}' \tag{14}$$

where $\hat{H}^{(0)}$ is the classical ground-state energy, $\hat{H}^{(2)}$ is a quadratic Bogoliubov–de Genes (BdG) bosonic Hamiltonian and $\hat{H}'$ represents higher order correction terms that describe magnon–magnon interactions. Finally, this BdG Hamiltonian is Fourier-transformed and diagonalized via a paraunitary matrix through a Bogoliubov transformation to find the magnon wavefunctions and spectrum.

An alternative yet equivalent approach is the so-called equation of motion (EOM) approach[21,38] in which the low-energy dynamics is captured by the small deviations of spins from their ordered directions :

$$\mathbf{s}_i \equiv \mathbf{S}_i - \langle \mathbf{S}_i \rangle \Rightarrow \mathbf{s}_i = \left(s_i^x, s_i^y, 0\right) \tag{15}$$

with $|\mathbf{s}_i| \ll \bar{S}_i$. By expanding the Hamiltonian in terms of the deviations, then considering their Heisenberg EOM, we reach a dynamical EOM that governs the spinwave dynamics:

$$-\mathrm{i}\frac{\mathrm{d}s_i^\alpha}{\mathrm{d}t} = \sum_{j,\beta} (\mathbf{M} \cdot \mathbf{R})_{i\alpha,j\beta} s_j^\beta \tag{16}$$

where $\mathbf{M}_{i\alpha,j\beta} = \delta_{i,j}(\sigma_y)^{\alpha,\beta}$ with σ_y is the y-Pauli matrix and $\mathbf{R}$ is a $2N \times 2N$, where N is the number of spins in the primitive magnetic unit cell, is a semi-positive-definite symmetric matrix that describes the spin–spin interactions and is referred to as the "magnon" Hamiltonian. The spectrum is then calculated as the eigenvalues of $\mathbf{M} \cdot \mathbf{R}$.

Fermionization map of LSW systems

For the calculation of the topological charges of the Weyl magnons, we used the numerical technique[37] after mapping the LSW Hamiltonian into its fermionic counterpart. An LSW problem can be mapped into a free-fermion system through the similarity transformation[38]:

$$\mathbf{H}_f = \sqrt{\mathbf{R}} \cdot \mathbf{M} \cdot \sqrt{\mathbf{R}} \tag{17}$$

where $\mathbf{R}$ is the magnon Hamiltonian in Eq. (16) of a generic spin-orbit coupled magnet, and $\mathbf{H}_f$ is the free-fermion Hamiltonian. Since $\mathbf{R}$ is a positive-definite matrix for a gapped LSW system, its square root is well-defined. The key feature is that $\mathbf{H}_f$ shares the same spectrum and band topology as the spinwave Hamiltonian. It also preserves the same symmetries of the magnon Hamiltonian, therefore if a unitary symmetry g of the magnetic order exists, its implementation on the magnon Hamiltonian takes the form $[O_g, \mathbf{R}] = 0$ and $[O_g, M] = 0$, where $O_g \in SO(2N)$ and the fermionic counterpart preserves it $O_g \mathbf{H}_f O_g^\dagger = \mathbf{H}_f$. For an anti-unitary symmetry p, $[O_p, \mathbf{R}] = 0$, $\{O_p, M\} = 0$, and the fermionic Hamiltonian $\mathbf{H}_f$ satisfies $O_p \mathbf{H}_f O_p^\dagger = -\mathbf{H}_f$.

Therefore, this mapping can be used as an additional route to apply the results of TQC and SI theories to the spinwave problem. In this mapping, a spinless electronic counterpart replaces the spinwave problem; the spinwave variables $S^\pm$ take the role of the atomic orbitals. Therefore, the band representation is induced from the site symmetry group of the spinwave variables. Thus, a tabulation[21,88] of the magnetic site symmetry groups compatible with the magnetic order and their representations provides a direct way to study the induced magnon band representation for a given $\mathcal{MSG}$ using MBANDREP[25,31] BCS tool as discussed in the text.

Data availability

No datasets were generated or analysed during the current study.

Code availability

The search program developed in this work to identify topological magnon compounds can be accessed through the following link: https://github.com/MohammedKaraki/topological-magnon-search to both facilitate the reproduction of our results and provide a tool for other researchers to investigate the magnon band topology in magnetic systems.

Received: 31 January 2025; Accepted: 14 June 2025;

References

1. Hasan, M. Z. & Kane, C. L. Colloquium: topological insulators. *Rev. Mod. Phys.* **82**, 3045–3067 (2010).
2. McClarty, P. A. Topological magnons: a review. *Annu. Rev. Condens. Matter Phys.* **13**, 171–190 (2022).
3. Chumak, A. V., Vasyuchka, V. I., Serga, A. A. & Hillebrands, B. Magnon spintronics. *Nat. Phys.* **11**, 453–461 (2015).
4. Zhuo, F., Kang, J., Manchon, A. & Cheng, Z. Topological phases in magnonics. *Adv. Phys. Res.* **n/a**, 2300054 (2024).
5. Zhang, T. et al. Catalogue of topological electronic materials. *Nature* **566**, 475–479 (2019).
6. Tang, F., Po, H. C., Vishwanath, A. & Wan, X. Comprehensive search for topological materials using symmetry indicators. *Nature* **566**, 486–489 (2019).
7. Vergniory, M. G. et al. A complete catalogue of high-quality topological materials. *Nature* **566**, 480–485 (2019).
8. Xu, Y. et al. High-throughput calculations of magnetic topological materials. *Nature* **586**, 702–707 (2020).
9. Su, Y. et al. High-throughput first-principle prediction of collinear magnetic topological materials. *npj Comput. Mater.* **8**, 261 (2022).
10. Robredo, I. et al. New magnetic topological materials from high-throughput search. Preprint at https://arxiv.org/abs/2408.16851 (2024).
11. Xu, Y. et al. Catalog of topological phonon materials. *Science* **384**, eadf8458 (2024).
12. Mook, H. A. & Nicklow, R. M. Neutron scattering investigation of the magnetic excitations in iron. *Phys. Rev. B.* **7**, 336–342 (1973).
13. Qin, H. et al. Long-living terahertz magnons in ultrathin metallic ferromagnets. *Nat. Commun.* https://www.nature.com/articles/ncomms7126 (2015).
14. Hirjibehedin, C. F., Lutz, C. P. & Heinrich, A. J. Spin coupling in engineered atomic structures. *Science* **312**, 1021–1024 (2006).
15. Mitrano, M., Johnston, S., Kim, Y.-J. & Dean, M. P. M. Exploring quantum materials with resonant inelastic x-ray scattering. *Phys. Rev. X* **14**, 040501 (2024).
16. Pelliciari, J. et al. Tuning spin excitations in magnetic films by confinement. *Nat. Mater.* **20**, 188–193 (2021).
17. Pelliciari, J. et al. Evolution of spin excitations from bulk to monolayer fese. *Nat. Commun.* https://doi.org/10.1038/s41467-021-23317-3 (2021).
18. Lebert, B. W. et al. Resonant inelastic x-ray scattering study of α-rucl3: a progress report. *J. Phys. Condens. Matter* **32**, 144001 (2020).
19. Brookes, N. B. et al. Spin waves in metallic iron and nickel measured by soft x-ray resonant inelastic scattering. *Phys. Rev. B.* **102**, 064412 (2020).
20. Chaix, L. et al. Resonant inelastic x-ray scattering studies of magnons and bimagnons in the lightly doped cuprate $\mathrm{la}_{2-x}\mathrm{sr}_x\mathrm{cuo}_4$. *Phys. Rev. B.* **97**, 155144 (2018).
21. Karaki, M. J. et al. An efficient material search for room-temperature topological magnons. *Sci. Adv.* **9**, eade7731 (2023).
22. Peng, B., Jiang, Y., Fang, Z., Weng, H. & Fang, C. Topological classification and diagnosis in magnetically ordered electronic materials. *Phys. Rev. B* https://doi.org/10.1103/PhysRevB.105.235138 (2022).
23. Po, H. C., Vishwanath, A. & Watanabe, H. Symmetry-based indicators of band topology in the 230 space groups. *Nat. Commun.* **8**, 50 (2017).
24. Bradlyn, B. et al. Topological quantum chemistry. *Nature* **547**, 298–305 (2017).
25. Elcoro, L. et al. Magnetic topological quantum chemistry. *Nat. Commun.* https://doi.org/10.1038/s41467-021-26241-8 (2021).
26. Cano, J. et al. Building blocks of topological quantum chemistry: elementary band representations. *Phys. Rev. B.* **97**, 035139 (2018).

27. Cano, J. & Bradlyn, B. Band representations and topological quantum chemistry. *Annu. Rev. Condens. Matter Phys.* **12**, 225–246 (2021).
28. Kruthoff, J., de Boer, J., van Wezel, J., Kane, C. L. & Slager, R.-J. Topological classification of crystalline insulators through band structure combinatorics. *Phys. Rev. X* **7**, 041069 (2017).
29. Bouhon, A., Lange, G. F. & Slager, R.-J. Topological correspondence between magnetic space group representations and subdimensions. *Phys. Rev. B.* **103**, 245127 (2021).
30. Khalaf, E., Po, H. C., Vishwanath, A. & Watanabe, H. Symmetry indicators and anomalous surface states of topological crystalline insulators. *Phys. Rev. X.* **8**, 031070 (2018).
31. Xu, Y. et al. High-throughput calculations of magnetic topological materials. *Nature* **586**, 702 – 707 (2020).
32. Gallego, S. V. et al. *MAGNDATA*: towards a database of magnetic structures. I. The commensurate case. *J. Appl. Crystallogr.* **49**, 1750–1776 (2016).
33. Li, F.-Y. et al. Weyl magnons in breathing pyrochlore antiferromagnets. *Nat. Commun.* **7**, 12691 (2016).
34. Mook, A., Henk, J. & Mertig, I. Tunable magnon weyl points in ferromagnetic pyrochlores. *Phys. Rev. Lett.* **117**, 157204 (2016).
35. Muñoz, A., Alonso, J. A., Martínez-Lope, M. J., García-Muñoz, J. L. & Fernández-Díaz, M. T. Magnetic structure evolution of Ndmno3 derived from neutron diffraction data. *J. Phys. Condens. Matter* **12**, 1361 (2000).
36. Kumar, A., Yusuf, S. M. & Ritter, C. Nd-ordering-driven mn spin reorientation and magnetization reversal in the magnetostructurally coupled compound $NdMno_3$. *Phys. Rev. B.* **96**, 014427 (2017).
37. Fukui, T., Hatsugai, Y. & Suzuki, H. Chern numbers in discretized Brillouin zone: efficient method of computing (spin) hall conductances. *J. Phys. Soc. Jpn.* **74**, 1674–1677 (2005).
38. Lu, F. & Lu, Y.-M. Magnon band topology in spin-orbital coupled magnets: classification and application to α-$rucl_3$. Preprint at https://arxiv.org/abs/1807.05232v2 (2018).
39. Henk, J. & Schattke, W. A subroutine package for computing Green's functions of relaxed surfaces by the renormalization method. *Comput. Phys. Commun.* **77**, 69–83 (1993).
40. Kunkemöller, S. et al. Highly anisotropic magnon dispersion in Ca_2RuO_4: evidence for strong spin orbit coupling. *Phys. Rev. Lett.* **115**, 247201 (2015).
41. Porter, D. G. et al. Magnetic anisotropy and orbital ordering in Ca_2RuO_4. *Phys. Rev. B.* **98**, 125142 (2018).
42. Cuono, G., Forte, F., Romano, A. & Noce, C. Emerging new phases in correlated mott insulator ca2ruo4. *J. Phys. Condens. Matter* **37**, 053002 (2024).
43. Kunnmann, W., Ferretti, A. & Wold, A. Flux growth of NiFe2O4 crystals by the Czochralski method. *J. Appl. Phys.* **34**, 1264–1264 (1963).
44. Shahi, P. et al. Transport, magnetic and structural properties of Mott insulator MnV2O4 at the boundary between localized and itinerant electron limit. *J. Mater. Sci.* **49**, 7317–7324 (2014).
45. El-Khatib, S. et al. Conduction via surface states in antiferromagnetic Mott-insulating Nis_2 single crystals. *Phys. Rev. Mater.* **5**, 115003 (2021).
46. Yao, X. & Honig, J. Growth of nickel dichalcogenides crystals with pyrite structure from tellurium melts [Nis2, Nis2-xSex (x ≤ 0.7)]. *Mater. Res. Bull.* **29**, 709–716 (1994).
47. Murakami, M. et al. Fabrication of multiferroic epitaxial BiCrO3 thin films. *Appl. Phys. Lett.* **88**, 152902 (2006).
48. Tian, C. et al. Dyocl: a rare-earth based two-dimensional van der Waals material with strong magnetic anisotropy. *Phys. Rev. B.* **104**, 214410 (2021).
49. Okada, S. et al. Crystal growth by molten metal flux method and properties of manganese silicides. *J. Alloy. Compd.* **317**, 315–319 (2001).
50. Kounta, I. et al. Competitive actions of MNSi in the epitaxial growth of Mn_5Si_3 thin films on Si (111). *Phys. Rev. Mater.* **7**, 024416 (2023).
51. Balbashov, A., Karabashev, S., Mukovskiy, Y. & Zverkov, S. Growth and giant magnetoresistance effect in LaCaMnO and LaSrMnO single crystals. *J. Cryst. Growth* **167**, 365–368 (1996).
52. Nakatsuji, S. & Maeno, Y. Synthesis and single-crystal growth of $Ca_{2-x}Sr_xRuO_4$. *J. Solid State Chem.* **156**, 26–31 (2001).
53. Morin, F. J. Magnetic susceptibility of αFe_2O_3 and αFe_2O_3 with added titanium. *Phys. Rev.* **78**, 819–820 (1950).
54. Yuan, S. J. et al. First-order spin reorientation transition and specific-heat anomaly in CeFeO3. *J. Appl. Phys.* **114**, 113909 (2013).
55. Glazkov, V. P., Kvardakov, V. V. & and, V. A. S. Pressure induced spin-reorientation transition in FeBO3. *High. Press. Res.* **17**, 179–185 (2000).
56. Xue, M. et al. Tailoring spin reorientation and magnetic interaction for room-temperature spintronics in TB-doped SmFeO3 single crystal. Preprint at https://arxiv.org/abs/2503.23086 (2025).
57. Ebrahimian, A., Dyrdał, A. & Qaiumzadeh, A. Control of magnetic states and spin interactions in bilayer CrCl3 with strain and electric fields: an ab initio study. *Sci. Rep.* https://doi.org/10.1038/s41598-023-32598-1 (2023).
58. Masciocchi, G. et al. Strain effects on magnetic compensation and spin reorientation transition of Co/Gd synthetic ferrimagnets. *J. Appl. Phys.* **134***,* 013904 (2023).
59. Kargeti, K., Sen, A. & Panda, S. K. Strain-induced electronic and magnetic transition in the antiferromagnetic spin chain compound lacrs $s=\frac{3}{2}$. *Phys. Rev. B.* **109**, 035125 (2024).
60. Nikitin, S. E. et al. Thermal evolution of Dirac magnons in the honeycomb ferromagnet $CrBr_3$. *Phys. Rev. Lett.* **129**, 127201 (2022).
61. Chernyshev, A. L. & Maksimov, P. A. Damped topological magnons in the kagome-lattice ferromagnets. *Phys. Rev. Lett.* **117**, 187203 (2016).
62. Zhitomirsky, M. E. & Chernyshev, A. L. Colloquium: spontaneous magnon decays. *Rev. Mod. Phys.* **85**, 219–242 (2013).
63. Mourigal, M., Zhitomirsky, M. E. & Chernyshev, A. L. Field-induced decay dynamics in square-lattice antiferromagnets. *Phys. Rev. B.* **82**, 144402 (2010).
64. Hong, T. et al. Field induced spontaneous quasiparticle decay and renormalization of quasiparticle dispersion in a quantum antiferromagnet. *Nat. Commun.* **8**, 15148 (2017).
65. Elliot, M. et al. Order-by-disorder from bond-dependent exchange and intensity signature of nodal quasiparticles in a honeycomb cobaltate. *Nat. Commun.* https://doi.org/10.1038/s41467-021-23851-0 (2021).
66. Scheie, A. et al. Dirac magnons, nodal lines, and nodal plane in elemental gadolinium. *Phys. Rev. Lett.* **128**, 097201 (2022).
67. Onose, Y. et al. Observation of the magnon Hall effect. *Science* **329**, 297–299 (2010).
68. Akazawa, M. et al. Topological thermal Hall effect of magnons in magnetic skyrmion lattice. *Phys. Rev. Res.* **4**, 043085 (2022).
69. Kim, H.-L. et al. Thermal Hall effects due to topological spin fluctuations in YMnO3. *Nat. Commun.* https://doi.org/10.1038/s41467-023-44448-9 (2024).
70. Shindou, R., Matsumoto, R., Murakami, S. & Ohe, J.-i Topological chiral magnonic edge mode in a magnonic crystal. *Phys. Rev. B.* **87**, 174427 (2013).
71. Halperin, B. I. Quantized Hall conductance, current-carrying edge states, and the existence of extended states in a two-dimensional disordered potential. *Phys. Rev. B.* **25**, 2185–2190 (1982).
72. Streib, S., Vidal-Silva, N., Shen, K. & Bauer, G. E. W. Magnon-phonon interactions in magnetic insulators. *Phys. Rev. B.* **99**, 184442 (2019).
73. Cong, A. et al. Exchange-mediated magnon-phonon scattering in monolayer CrI_3. *Phys. Rev. B.* **106**, 214424 (2022).
74. Malz, D., Knolle, J. & Nunnenkamp, A. Topological magnon amplification. *Nat. Commun.* https://doi.org/10.1038/s41467-019-11914-2 (2019).
75. Corticelli, A., Moessner, R. & McClarty, P. A. Spin-space groups and magnon band topology. *Phys. Rev. B.* **105**, 064430 (2022).

76. Yang, J., Liu, Z.-X. & Fang, C. Symmetry invariants and classes of quasi-particles in magnetically ordered systems having weak spin-orbit coupling *Nat. Commun.* **15***,* 10203 (2024).
77. Schiff, H., Corticelli, A., Guerreiro, A., Romhányi, J. & McClarty, P. The crystallographic spin point groups and their representations. *SciPost Phys.* **18***,* 109 (2025).
78. Chen, X. et al. Enumeration and representation theory of spin space groups. *Phys. Rev. X* **14**, 031038 (2024).
79. Chen, X. et al. Unconventional magnons in collinear magnets dictated by spin space groups. *Nature* https://www.nature.com/articles/s41586-025-08715-7 (2025).
80. Šmejkal, L., Sinova, J. & Jungwirth, T. Emerging research landscape of altermagnetism. *Phys. Rev. X* **12**, 040501 (2022).
81. Krempaský, J. et al. Altermagnetic lifting of Kramers spin degeneracy. *Nature* **626**, 517–522 (2024).
82. Takahashi, R. & Nagaosa, N. Berry curvature in magnon-phonon hybrid systems. *Phys. Rev. Lett.* **117**, 217205 (2016).
83. Go, G., Kim, S. K. & Lee, K.-J. Topological magnon-phonon hybrid excitations in two-dimensional ferromagnets with tunable Chern numbers. *Phys. Rev. Lett.* **123**, 237207 (2019).
84. Zhang, X., Zhang, Y., Okamoto, S. & Xiao, D. Thermal Hall effect induced by magnon-phonon interactions. *Phys. Rev. Lett.* **123**, 167202 (2019).
85. Bao, S. et al. Direct observation of topological magnon polarons in a multiferroic material. *Nat. Commun.* **14**, 6093 (2023).
86. Bradlyn, B. et al. Band connectivity for topological quantum chemistry: Band structures as a graph theory problem. *Phys. Rev. B.* **97**, 035138 (2018).
87. Zak, J. Band representations and symmetry types of bands in solids. *Phys. Rev. B.* **23**, 2824–2835 (1981).
88. Corticelli, A., Moessner, R. & McClarty, P. A. Identifying and constructing complex magnon band topology. *Phys. Rev. Lett.* **130**, 206702 (2023).
89. Bao, S. et al. Discovery of coexisting Dirac and triply degenerate magnons in a three-dimensional antiferromagnet. *Nature Commun.* https://doi.org/10.1038/s41467-018-05054-2 (2018).
90. Yuan, B. et al. Dirac magnons in a honeycomb lattice quantum *XY* magnet $CoTiO_3$. *Phys. Rev. X* **10**, 011062 (2020).
91. Chen, L. et al. Topological spin excitations in honeycomb ferromagnet CrI_3. *Phys. Rev. X* **8**, 041028 (2018).

Acknowledgements

Authors would like to thank Prof. Rolando Valdes Aguilar for helpful discussions. AEF acknowledges Dr. Xu Yang (OSU), Dr. Yufei Li (OSU) and Mr. Mohamed Nawwar (OSU) for fruitful discussions.

Author contributions

M.J.K designed, implemented the search algorithm and summarized its results in the Supplementary Materials. A.E.F thoroughly analyzed the algorithm results with the help of A.J.W, S.H, J.G, M.J.K and Y.M.L. Bulk and surface calculations along with band topology analyses were carried out by A.E.F. Manuscript was prepared by A.E.F. with input from A.J.W., M.J.K., Y.M.L., S.H. and J.G. Manuscript was edited by A.E.F. and Y.M.L. All authors contributed to the scientific discussion. Y.M.L. supervised the project. Mohammed J. Karaki and Ahmed E. Fahmy contributed equally to this work.

Competing interests

The authors declare no competing interests.

Additional information

Supplementary information The online version contains supplementary material available at https://doi.org/10.1038/s41524-025-01706-2.

Correspondence and requests for materials should be addressed to Mohammed J. Karaki, Ahmed E. Fahmy or Yuan-Ming Lu.